

QATAR EXOPLANET SURVEY: QATAR-6B – A GRAZING TRANSITING HOT JUPITER

KHALID ALSUBAI,¹ ZLATAN I. TSVETANOV,¹ DAVID W. LATHAM,² ALLYSON BIERYLA,²
GILBERT A. ESQUERDO,² DIMITRIS MISLIS,¹ STYLIANOS PYRZAS,¹ EMMA FOXELL,^{3,4}
JAMES MCCORMAC,^{3,4} CHRISTOPH BARANEC,⁵ NICOLAS P. E. VILCHEZ,¹ RICHARD WEST,^{3,4}
ALI ESAMDIN,⁶ ZHENWEI DANG,⁶ HANI M. DALEE,¹ AMANI A. AL-RAJHI,⁷ AND ABEER KH. AL-HARBI⁸

¹*Qatar Environment and Energy Research Institute (QEERI), HBKU, Qatar Foundation, PO Box 5825, Doha, Qatar*

²*Harvard-Smithsonian Center for Astrophysics, 60 Garden Street, Cambridge, MA 02138, USA*

³*Department of Physics, University of Warwick, Gibbet Hill Road, Coventry CV4 7AL, UK*

⁴*Centre for Exoplanets and Habitability, University of Warwick, Gibbet Hill Road, Coventry CV4 7AL, UK*

⁵*Institute for Astronomy, University of Hawai‘i at Mānoa, Hilo, HI 96720-2700, USA*

⁶*Xinjiang Astronomical Observatory, Chinese Academy of Sciences, 150 Science 1-Street, Urumqi, Xinjiang 830011, China*

⁷*Qatar Secondary Independent High School, Doha, Qatar*

⁸*Al-Kawthar Secondary Independent High School, Doha, Qatar*

(Received Oct 6, 2017; Revised Dec 4, 2017; Accepted Dec 5, 2017)

Submitted to AJ

ABSTRACT

We report the discovery of Qatar-6b, a new transiting planet identified by the Qatar Exoplanet Survey (QES). The planet orbits a relatively bright ($V=11.44$), early-K main-sequence star at an orbital period of $P \sim 3.506$ days. An SED fit to available multi-band photometry, ranging from the near-UV to the mid-IR, yields a distance of $d = 101 \pm 6$ pc to the system. From a global fit to follow-up photometric and spectroscopic observations, we calculate the mass and radius of the planet to be $M_p = 0.67 \pm 0.07 M_J$ and $R_p = 1.06 \pm 0.07 R_J$ respectively. We use multi-color photometric light curves to show that the transit is grazing, making Qatar-6b one of the few exoplanets known in a grazing transit configuration. It adds to the short list of targets that offer the best opportunity to look for additional bodies in the host planetary system through variations in the transit impact factor and duration.

Keywords: techniques: photometric - planets and satellites: detection - planets and satellites: fundamental parameters - planetary systems.

1. INTRODUCTION

Dedicated ground-based photometric surveys continue to provide a steady supply of short period, transiting exoplanets orbiting relatively bright stars. Subsequent studies of hot Jupiters and other close-orbiting large planets – a type of planets not present in our solar system – contribute key information towards understanding the overall structure and composition of planetary systems.

Over the past two decades, transiting exoplanets have been the subject of a number of different studies, yielding a wide range of results, including identifying the presence of additional bodies using transit-time variations (e.g., Agol et al. 2005, Holman & Murray 2005); detection of thermal emission (e.g., Charbonneau et al. 2005, Deming et al. 2005, Deming et al. 2006); spin-orbit alignment or lack thereof (e.g., Albrecht et al. 2012, see also Winn & Fabrycky 2015 for a review) and studies of exoplanets’ atmospheres (e.g., Charbonneau et al. 2002, Tinetti et al. 2007, Sing et al. 2016) to name but a few.

Although space-based surveys have dramatically increased the number of (fully) transiting exoplanets, *grazing* (or nearly- so) transiting exoplanets still constitute only a tiny fraction of the known exoplanet population. In fact, to the best of our knowledge, their number has only recently reached double-digits; systems identified by ground-based surveys are WASP-34b (Smalley et al. 2011); WASP-45b (Anderson et al. 2012); WASP-67b (Hellier et al. 2011); WASP-140b (Hellier et al. 2017) and HAT-P-27b/WASP-40b (Béky et al. 2011/Anderson et al. 2011), coupled with the space-based detections of CoRoT-25b (Almenara et al. 2013); CoRoT-33b (Cszimadia et al. 2015); Kepler-434b (Almenara et al. 2015); Kepler-447b (Lillo-Box et al. 2015) and K2-31b (Grziwa et al. 2016) to complete the, rather small, family of ten.

Planets in grazing transit configurations offer an intriguing, yet hitherto untested, avenue of study (Lillo-Box et al. 2015). In short, any external gravitational influence on the system, e.g., the presence

of additional bodies such as an outer planet or even an exo-moon, would perturb the grazing planet’s orbit and could potentially induce periodic variations of the transit impact parameter (TIP, Kipping 2009), leading to transit duration variations (TDV, Kipping 2010). With sufficient cadence and photometric accuracy, these variations would be detectable in the transit light curve, and could be used in turn to study the perturbing body.

In this paper we present the discovery of Qatar-6b, a newly found hot Jupiter on a grazing transit. The paper is organized as follows: in Section 2 we present the survey photometry and describe the follow-up spectroscopy and photometry used to confirm the planetary nature of the transits. In Section 3 we present analysis of the data and the global system solutions using simultaneous fits to the available RV and follow-up photometric light curves, and in Section 4 we summarize the results.

2. OBSERVATIONS

2.1. *Discovery photometry*

The survey data were collected with the Qatar Exoplanet Survey (QES) hosted by the New Mexico Skies Observatory¹ located at Mayhill, NM, USA. A full description of QES can be found in our previous publications, e.g., Alsubai et al. (2013), Alsubai et al. (2017). For completeness, here we give the main survey characteristics. QES uses two overlapping wide field 135 mm (f/2.0) and 200 mm (f/2.0) telephoto lenses, along with four 400 mm (f/2.8) telephoto lenses, mosaiced to image an $11^\circ \times 11^\circ$ field on the sky simultaneously at three different pixel scales — 12, 9 and 4 arc-sec, respectively, for the three different focal length lenses. All lenses are equipped with FLI ProLine PL6801 cameras, with KAF-1680E 4k×4k detectors. Exposure times are 60 s, for each of the four CCDs attached to the 400 mm lenses; 45 s, for the CCD equipped with the 200 mm lens; and 30 s, for the CCD equipped with the 135 mm lens. The com-

¹ <http://www.nmskies.com>

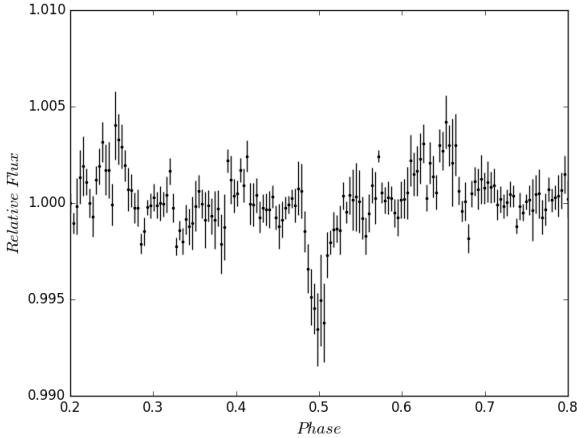


Figure 1. The discovery light curve for Qatar-6b phase folded with the BLS estimated period, as it appears in the QES archive.

bination of large aperture lenses and high survey angular resolution, allow QES to reach 1% photometric precision up to 13.5-14.0 mag stars.

The data were reduced with the QES pipeline, which performs bias-correction, dark-current subtraction and flat-fielding in the standard fashion, while photometric measurements are extracted using the image subtraction algorithm by [Bramich \(2008\)](#); a more detailed description of the pipeline is given in [Alsubai et al. \(2013\)](#).

The output light curves are ingested into the QES archive and subjected to a combination of the Trend Filtering Algorithm (TFA, [Kovács et al. 2005](#)) and the Doha algorithm ([Mislis et al. 2017](#)), to model and remove systematic patterns of correlated noise. Transit-like events are identified using the Box Least Squares algorithm (BLS) of [Kovács et al. \(2002\)](#), during a candidates search on the archive light curves following the procedure described in [Collier et al. \(2006\)](#). We note that the initial candidate selection is an automatic procedure, but the final vetting is done by eye. The BLS algorithm provided a tentative ephemeris which was used to phase-fold the discovery light curve shown in Figure 1. The discovery light curve of Qatar-6b contains 2324 data points obtained from March to July 2012.

The host of Qatar-6b is a $V = 11.44$ mag ($B = 12.34$ mag) high proper motion star (TYC 1484-434-1, 2MASS J14485047+2209093, henceforth designated Qatar-6) of spectral type close to K2V. A detailed discussion of stellar parameters based on the analysis of our follow-up spectra and on the available photometry is presented in Section 3.1. Here we note only that the host star spectral type is initially estimated from a multi-color (V , J , H and K bands) fit to the magnitudes, using a standard Random-Forest classification algorithm, trained with ~ 2000 standards with spectral types ranging from early A to late M.

2.2. Follow-up photometry

Follow-up photometric observations for Qatar-6b were collected with the 1.2 m telescope at the Fred L. Whipple Observatory (FLWO, Mount Hopkins, Arizona) using KeplerCam, a single $4K \times 4K$ CCD that covers an area of $23' \times 23'$ on the sky. The target was observed on four occasions – (1) on the night of January 30, 2017 through Sloan i filter; (2) on May 5, 2017 (Sloan i); (3) on May 19, 2017 (Sloan r); and (4) on June 9, 2017 (Sloan z).

Two additional transits were obtained using the Near Infra-red Transiting ExoplanetS telescope (NITES, [McCormac et al. 2014](#)) located at the Observatorio del Roque de los Muchachos (ORM, La Palma, Canary Islands), on March 9, 2017 and on March 23, 2017. On both nights, a total of 354 30 s images were obtained with a Johnson-Bessel V -band filter. The data were reduced in PYTHON using CCDPROC ([Craig et al. 2015](#)). A master bias, dark and flat was created using the standard process on each night. A minimum of 21 of each frame was used in each master calibration frame. Non-variable nearby comparison stars were selected by hand and aperture photometry extracted using SEP ([Barbary 2016](#); [Bertin & Arnouts 1996](#)).

Figure 2 shows the follow-up light curves together with the model fits described in Section 3.5.

2.3. Follow-up spectroscopy

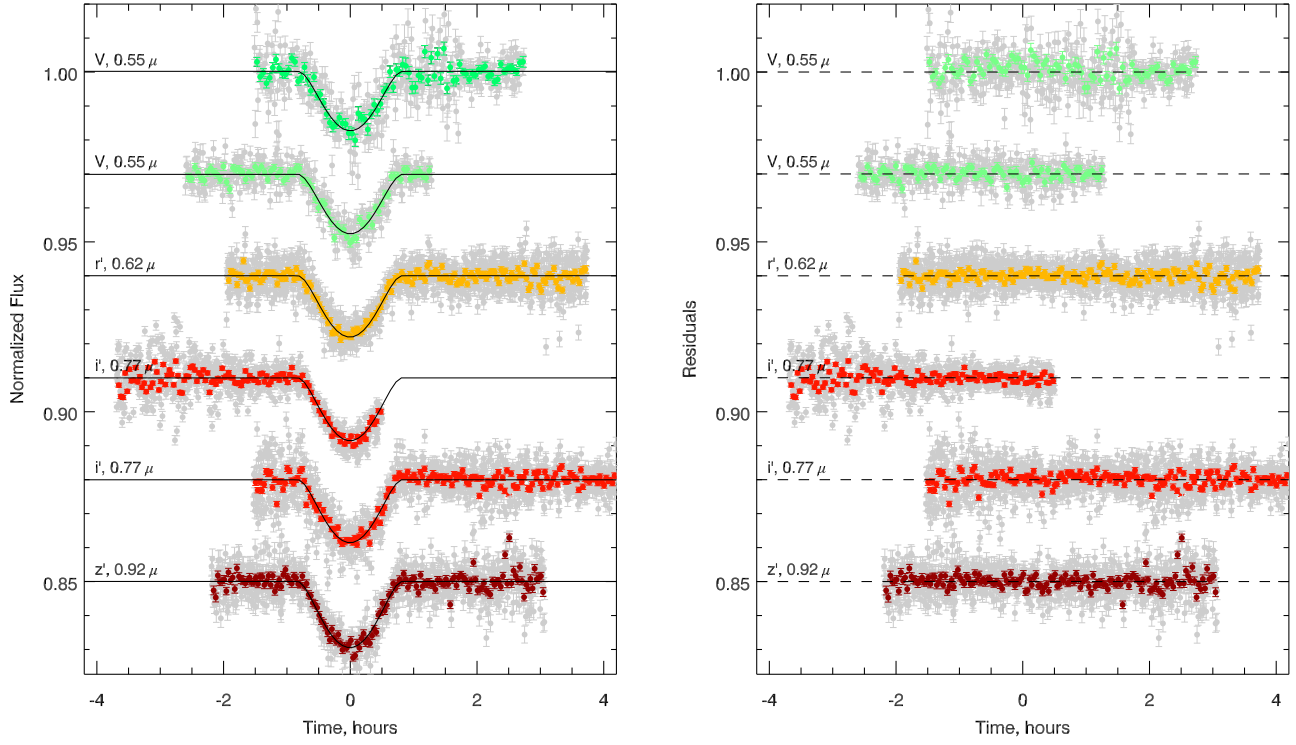


Figure 2. The six follow-up light curves of Qatar-6b. The *left* panel shows the light curves ordered from top to bottom in increasing filter wavelength (the light curves have been shifted vertically for clarity). The original observational data points are plotted in light gray and binned data are shown in darker colors (see Section 3.4). The solid, black lines represent the best model fit for the corresponding filter. The residuals from the fits are shown in the *right* panel. The dates of observations for each light curve are given in the text.

Similar to our campaigns for all QES candidates, follow-up spectroscopic observations were obtained with the Tillinghast Reflector Echelle Spectrograph (TRES) on the 1.5 m Tillinghast Reflector at the FLWO. We used TRES in a configuration with the medium fiber, which yields a resolving power of $R \sim 44,000$, corresponding to a velocity resolution element of 6.8 km s^{-1} FWHM. The spectra were extracted using version 2.55 of the code described in Buchhave et al. (2010). The wavelength calibration for each spectrum was established using exposures of a thorium-argon hollow-cathode lamp illuminating the science fiber, obtained immediately before and after each observation of the star.

For Qatar-6 a total of 34 spectra were obtained between April 13 – May 31, 2016 with exposure times ranging from 450 sec to 1600 sec and an average signal-to-noise ratio per resolution element (SNRe) of ~ 36 at the peak of the continuum in the echelle order centered on the Mg b triplet near 519 nm. Relative radial velocities (RV) were derived by cross-correlating each observed spectrum against the strongest exposure of the same star, order by order for a set of echelle orders selected to have good SNRe and minimal contamination by telluric lines introduced by the Earth’s atmosphere. These RVs are reported in Table 1 (with the time values in Barycentric Julian Date in Barycentric Dynamical time, BJD_{TDB}) and plotted in Figure 3. The observation that was used for the template

spectrum has, by definition, a RV of 0.0 km s^{-1} . The error on the template RV is defined as the smallest error of all the other errors. We also derived values for the line profile bisector spans (BS, lower panel in Figure 3), to check for astrophysical phenomena other than orbital motion that might produce a periodic signal in the RVs with the same period as the photometric ephemeris for the transits. The procedures used to determine RVs and BSs are outlined in [Buchhave et al. \(2010\)](#).

To get the absolute center-of-mass velocity for the system (γ), we have to provide an absolute velocity for the observation that was used for the template when deriving the relative velocities. To derive an absolute velocity for that observation, we correlate the Mg b order against the template from the CfA library of synthetic templates that gives the highest peak correlation value. Then we add the relative γ -velocity from the orbital solution, and also correct by -0.61 km s^{-1} , mostly because the CfA library does not include the gravitational redshift. This offset has been determined empirically by many observations of IAU Radial Velocity Standard Stars. We quote an uncertainty in the resulting absolute velocity of $\pm 0.1 \text{ km s}^{-1}$, which is an estimate of the residual systematic errors in the IAU Radial Velocity Standard Star system.

3. ANALYSIS AND RESULTS

3.1. Host star spectroscopic parameters

To derive the host star characteristics, we analyzed the TRES spectra using the Stellar Parameter Classification (SPC) tool developed by [Buchhave et al. \(2012\)](#). The SPC cross correlates the observed spectrum with a library of synthetic spectra from Kurucz model atmospheres and finds the stellar parameters from a multi-dimensional surface fit to the peak correlation values. We used the ATLAS9 grid of models with the Opacity Distribution Functions from [Castelli & Kurucz \(2004\)](#). The SPC determined stellar parameters — effec-

Table 1. Relative RVs and BS variations for Qatar-6.

BJD _{TDB}	RV (m s^{-1})	BS (m s^{-1})
2457491.849996	228 ± 13	-29 ± 11
2457496.967581	100 ± 20	4 ± 10
2457498.832531	246 ± 10	8 ± 9
2457499.810664	174 ± 11	-18 ± 10
2457500.837013	73 ± 17	10 ± 11
2457501.797354	152 ± 12	10 ± 9
2457503.847470	95 ± 17	-15 ± 12
2457504.813571	114 ± 16	14 ± 15
2457505.818142	234 ± 17	7 ± 13
2457506.856937	233 ± 20	19 ± 15
2457507.778682	67 ± 18	-17 ± 13
2457508.762515	153 ± 12	-8 ± 11
2457509.702250	253 ± 13	-11 ± 14
2457510.768550	85 ± 12	-27 ± 9
2457511.766238	0 ± 16	-3 ± 9
2457512.758133	201 ± 15	-28 ± 13
2457513.838902	185 ± 14	-41 ± 9
2457514.828265	65 ± 13	-5 ± 12
2457523.750772	253 ± 18	-25 ± 12
2457524.927611	103 ± 17	5 ± 27
2457526.718970	272 ± 20	7 ± 12
2457527.732882	240 ± 17	24 ± 17
2457528.683977	90 ± 18	50 ± 13
2457529.693135	142 ± 14	30 ± 12
2457530.685060	272 ± 19	25 ± 12
2457531.877658	121 ± 20	73 ± 18
2457532.735667	24 ± 18	1 ± 11
2457533.795727	201 ± 20	-29 ± 16
2457534.750027	215 ± 12	24 ± 10
2457535.933783	84 ± 30	33 ± 28
2457536.677373	83 ± 11	-24 ± 16
2457537.707875	232 ± 14	-36 ± 13
2457538.752114	95 ± 15	-12 ± 9
2457539.781151	55 ± 15	-16 ± 11

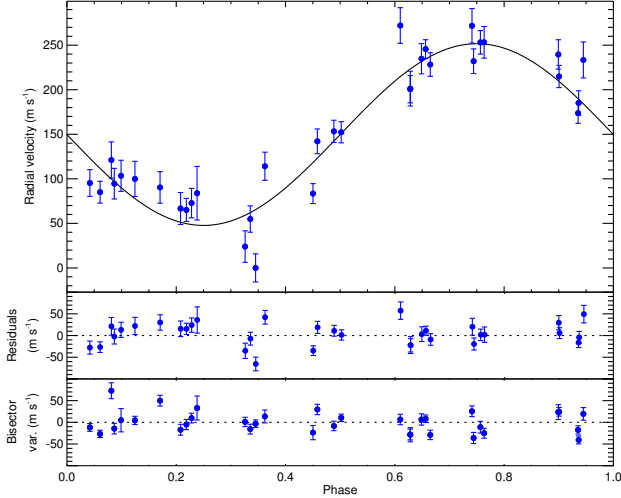


Figure 3. Orbital solution for Qatar-6b, showing the velocity curve and observed velocities and the bisector values.

tive temperature (T_{eff}), metallicity ($[m/H]^2$), surface gravity ($\log g$), and projected rotational velocity $v \sin i$ — are given in Table 2. These values are calculated by averaging the stellar parameters derived for each spectrum individually and weighted by the height of the cross-correlation function. T_{eff} , $\log g$, and $[m/H]$ are then used as input parameters for the Torres relations (Torres et al. 2010) to derive estimates for the stellar mass and radius, yielding $M_{\star} = 0.820 M_{\odot}$ and $R_{\star} = 0.714 R_{\odot}$.

The host star age is an important parameter for understanding the evolution of exoplanetary systems. We estimate the age of Qatar-6 using both the gyrochronology and isochrone fitting methods. For the gyrochronology age, we followed the formalism of Brown (2014) assuming the stellar rotation axis is perpendicular to the orbital plane. There are four equations in Brown’s work describing the rotational period-color-age relation — in our case, equations 2, 3, and 4 give consistent estimates of the star’s age, while eq. 1 (based on the $B - V$ color, see Section 3.2) gives about half the

value. The uncertainty of the age estimate is entirely dominated by the errors in determining the stellar rotation ($\pm 0.5 \text{ km s}^{-1}$) leading to age estimates, τ_{gyr} , in the range 0.75–1.5 Gyr (eq. 2, 3 and 4) and 0.4–0.6 Gyr (eq. 1).

Additionally, using the model isochrones from the Dartmouth database (Dotter et al. 2008) and input parameters from Table 4, we calculate an independent value for the age of the host star as $\tau_{\text{iso}} \approx 1.0$ Gyr. Furthermore, the global solution for the system parameters presented in Section 3.5, which uses the YY isochrones (Yi et al. 2001), gives a star age of $\tau_{\text{iso}} = 1.02 \pm 0.62$ Gyr. In Table 2 we quote the age of the host star as 1 Gyr, which is where all our estimates converge and put the uncertainty conservatively at 0.5 Gyr.

3.2. SED fit and distance determination

The host star of Qatar-6b has been observed by a number of imaging surveys covering the entire wavelength range $0.23 - 22 \mu\text{m}$, i.e. from the GALEX NUV to the WISE IR bands. The wide wavelength coverage combined with the parameters of the star derived from our spectroscopy provide an excellent base for a robust distance estimate based on a Spectral Energy Distribution (SED) fit.

However, inspection of the available data revealed that the target star is heavily saturated in many of the photometric bands covering the optical region ($\sim 0.4 \mu\text{m} - 1.0 \mu\text{m}$), particularly in the automated surveys, such as Pan-STARRS (PS1³), where the star is saturated to such a degree in all survey bands (g, r, i, z, y), that no magnitude values are available.

In SDSS (DR13, Albareti et al. 2016) measurements of the stellar magnitudes are provided, but there are clearly problems in some of the bands. For example, SDSS quotes a z -band value 2 magnitudes fainter than the quoted i -band value, which is completely unrealistic for a star with $T_{\text{eff}} \sim 5000$

² Note: The SPC determines metallicity as $[m/H]$, i.e., the total metal content is adjusted while individual elements abundances are kept fixed at the solar ratios.

³ <https://panstarrs.stsci.edu/>

Table 2. Basic observational parameters of Qatar-6b host star and photometry used for the SED fit.

Parameter	Description	Value	Source	Ref.
Names				
	225-118642 (UCAC3), TYC 1484-434-1			
	SDSS J144850.45+220909.2, 2MASS J14485047+2209093			
	GALEX J14485047+2209091, WISE J14485047+2209091			
Astrometry				
α_{2000}	RA (J2000)	$14^{\text{h}}48^{\text{m}}50.42^{\text{s}}$	GAIA	1
δ_{2000}	DEC (J2000)	$+22^{\circ}09'09.40''$	GAIA	1
μ_{α}	Proper motion, R.A., mas yr $^{-1}$	-51.9 ± 1.1	GAIA	1
μ_{δ}	Proper motion, DEC, mas yr $^{-1}$	14.8 ± 1.1	GAIA	1
Photometry				
NUV	GALEX NUV, mag	18.65 ± 0.03	GALEX	2
B	Johnson B , mag	12.389 ± 0.046	APASS	7
V	Johnson V , mag	11.438 ± 0.080	APASS	7
u	Sloan u , mag	13.892 ± 0.02	SDSS	3
g	Sloan g , mag	11.845 ± 0.02	SDSS	4
r	Sloan r , mag	11.070 ± 0.03	this work	
i	Sloan i , mag	10.91 ± 0.05	this work	
z	Sloan z , mag	10.76 ± 0.05	this work	
J	2MASS J , mag	9.711 ± 0.028	2MASS	5
H	2MASS H , mag	9.307	2MASS	5
K_s	2MASS K_s , mag	9.225	2MASS	5
W1	WISE1, mag	9.018 ± 0.022	WISE	6
W2	WISE2, mag	9.078 ± 0.020	WISE	6
W3	WISE3, mag	9.059 ± 0.022	WISE	6
W4	WISE4, mag	9.405 ± 0.405	WISE	6
Spectroscopic parameters				
	Spectral type	K2V	this work	
γ_{abs}	Systemic velocity, km s $^{-1}$	-27.864 ± 0.1	this work	
$v \sin i$	Rotational velocity, km s $^{-1}$	2.9 ± 0.5	this work	
P_{rot}	Rotation period, days	12.75 ± 1.75	this work	
τ	Age, Gyr	1.0 ± 0.5	this work	
A_V	Extinction, mag	0.093 ± 0.003	S&F2011	8
d	Distance, pc	101 ± 6	this work	

References—(1) GAIA DR1 <http://gea.esac.esa.int/archive/>, (2) GALEX <http://galex.stsci.edu/>, (3) Pickles & Depagne (2010), (4) SDSS DR13 Albareti et al. (2016), (5) 2MASS <http://irsa.ipac.caltech.edu/Missions/2mass.html>, (6) WISE <http://irsa.ipac.caltech.edu/Missions/wise.html>, (7) APASS <https://www.aavso.org/apass>, (8) Schlafly & Finkbeiner (2011)

K, as indicated by our spectra. Similarly, the u -band value is quoted to be 3 magnitudes fainter than the g -band, which is again not realistic for the type of star we expect and the low extinction in the direction of the object (Schlafly & Finkbeiner 2011).

To rectify this situation, we used our follow-up observations with KeplerCam taken in the Sloan r , i , and z bands to measure the magnitudes ourselves. This was achieved in the following fashion: for each band we selected images based on two criteria for the stellar profile, (i) $\text{FWHM} \leq 1.8''$ ($\leq 2.0''$ for the r -band) and (ii) ellipticity ≤ 0.1 . These limits were a compromise between the actual data quality and the need to have an adequate number of images on the one hand; and the requirement that the best images are selected on the other. The above cuts typically left us with 20-30% of the total images in each filter. These images were subsequently aligned and co-added, creating three master frames with equivalent exposure times of 12, 11, and 23 min for the r , i , and z band, respectively.

We then measured the magnitude of our target in each of the three master images through differential photometry using 11 stars in its immediate vicinity which were not saturated in the SDSS survey. Our measurements compare well with the spectrally matched magnitudes of Tyco 2 stars (Pickles & Depagne 2010) in the r and i bands, and are within 0.2 mag for the z band. In the r band the SDSS estimate, the spectrally matched value, and our measurement are within 0.1 mag, and the g band magnitudes given by SDSS and Pickles & Depagne (2010) are indistinguishable. For this reason, for the SED analysis we used the u and g magnitudes from Pickles & Depagne (2010) and our measurements for the r , i and z bands.

In the B and V bands, independent measurements are available from the APASS survey and can also be derived from the Tycho B_T and V_T magnitudes using the Bessell (2000) relations. The TASS photometric catalog (Droege et al. 2006) gives an ad-

ditional independent V band estimate. Most notably, the three V band values are consistent to within 0.03 mag, but the B band measurements from APASS and Tycho differ by 0.44 mag. We note here, that the Tycho measurements have substantial errors ($\sigma_{B_T} = 0.302$ and $\sigma_{V_T} = 0.124$) leading to a very uncertain $B - V$ color. Because of stated large uncertainties in the Tycho B_T and V_T magnitudes we adopted the B and V APASS values as representative of the true brightness of the host star in these bands. We note also that the spectrally matched B and V magnitudes from Pickles & Depagne (2010) are very close to the APASS values.

Table 2 presents the basic observational — astrometric, photometric and spectroscopic — parameters of Qatar-6b host star. We used these broadband measurements combined with the stellar radius R_* derived from the Torres relations to fit an SED using the NextGen library of theoretical models and solve for the extinction and distance. We imposed a prior of maximum extinction $A_V = 0.1$ mag as suggested by the Galactic dust reddening maps (Schlafly & Finkbeiner 2011). Figure 4 shows that the SED of a $T_{\text{eff}} \sim 5000$ K main sequence star fits well the broadband photometry for a distance $d = 101$ pc and minimal extinction ($A_V = 0.05$ mag) with a possible exception of the flux in the GALEX NUV band.

We note that the distance determined from the SED fit compares well with the estimated photometric distance. Assuming an absolute magnitude for the host star $M_V = 6.19$ (K2V, Pecaut & Mamajek 2013), extinction $A_V = 0.05$, and apparent magnitude $V = 11.438 \pm 0.08$ (Table 2) yields photometric distance $d_{\text{phot}} = 101\text{-}104$ pc.

3.3. The close-by object

Inspection of our KeplerCam follow-up data readily revealed a neighboring object, approximately $4''.5$ due South from the primary star. This object is naturally blended with the primary in the QES survey images, because of the coarse pixel size, but it is clearly visible and detected in all surveys with good spatial resolution imag-

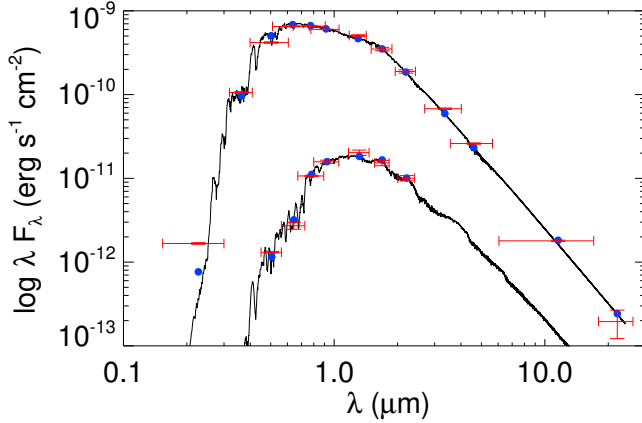


Figure 4. *Upper curve:* Spectral Energy Distribution (SED) fit for Qatar-6b host star. Photometric measurements, summarized in Table 2, are plotted as error bars, where the vertical error bars are the 1σ uncertainties, whereas the horizontal bars denote the effective width of the passbands. The solid curve is the best fit SED from the NextGen models where stellar parameters R_* , T_{eff} , $\log g$, and $[\text{Fe}/\text{H}]$ were kept fixed at the values derived from the global fit (Table 4), and visual extinction (A_V) and distance (d) were allowed to vary. *Lower curve* is the SED fit for the companion under the assumptions described in 3.3.

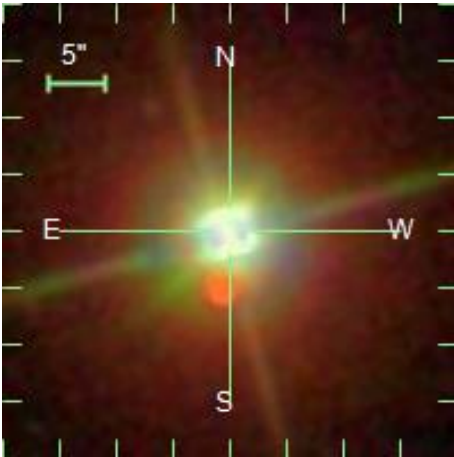


Figure 5. SDSS color composite image of Qatar-6b host star and neighboring object.

ing data (PanSTARRS, SDSS and 2MASS). An SDSS composite image of our target star and the neighboring object is shown in Figure 5.

In the SDSS, the object is classified as a galaxy and even a photometric redshift is given in the catalog. However, the object is located in the wings of a heavily saturated PSF and given the problems with estimating correct magnitudes of the primary star in at least some of the survey bands, the quoted values for this neighboring object are also suspect.

To address this problem we used the master KeplerCam frames, from the follow-up observations described above, to measure the neighbor/primary flux ratio. We employed two methods: (1) a PSF, determined from several isolated stars in close proximity to the target was aligned with the primary, scaled and subtracted; (2) a postage-stamp image centered on the primary was cut out, flipped along the y-axis, then aligned and subtracted from the original. Both methods allowed us to isolate the neighboring object and measure its flux using aperture photometry. This flux was then compared with the flux from the primary measured in matching aperture radii. To avoid substantial contamination from residuals from the subtraction we used 3 and 4 pixel aperture radius. We measured flux ratios of $F_{\text{neighbor}}/F_{\text{primary}} = 0.0049, 0.0146, 0.0266$ in the Sloan r, i and z bands respectively, corresponding to magnitude differences of $\Delta m = 5.80, 4.59$, and 3.94 mag. In addition, we note that at the limit of KeplerCam images resolution ($1''.8$) we do not detect departure from the PSF.

To further investigate the nature of the neighboring object we used the NIRC2 infrared camera behind the Keck II NGS AO system on 2017 August 3 to obtain differential near-infrared photometry of the companion and to examine its shape. We operated NIRC2 in its $9.95 \text{ mas pixel}^{-1}$ mode (Service et al. (2016)) which results in a field of view of $\sim 10''$. We used the J, H and K filters and obtained 2-point dithered images, for sky subtraction, with total exposure times of 40 s in each filter. We calibrated the images with dome flat-fields taken during the day. Figure 6 shows half of the sky subtracted NIRC2 AO frame (dithered position 1).

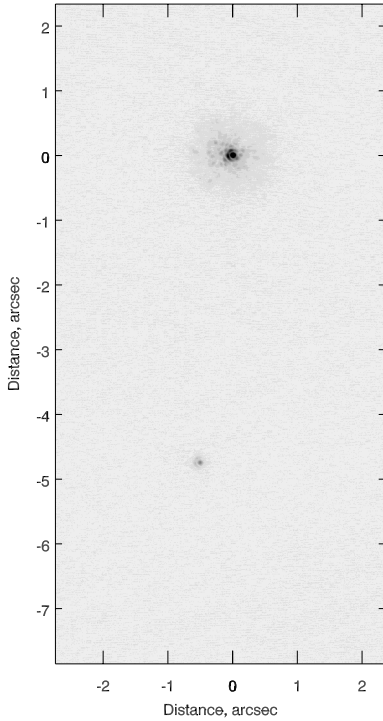


Figure 6. NIRC2 Keck AO image of Qatar-6b host star and its neighbor. Shown is one half the sky subtracted, flat field corrected dithered position 1. The image is stretched by the square root of the intensity to highlight the Airy rings.

The AO images show, without a doubt, the companion object is a star – the first two Airy rings of the diffraction limited PSF are clearly visible in all three filters. The flux ratio was measured separately from the two dithered positions and the results were averaged. We note that flux ratios determined from the two dithered positions are constant to within the measurements uncertainties for all aperture radii between $R_{\text{ap}} = 0''.3 - 0''.7$. The estimated values in the J , H and K bands are $F_{\text{neighbor}}/F_{\text{primary}} = 0.0382, 0.0438, 0.0512$ respectively, corresponding to magnitude differences $\Delta m = 3.54, 3.40$, and 3.19 mag.

From the flux ratio measurements described above we derive the apparent magnitudes of the companion object — 17.02, 15.49, 14.69, 13.26, 13.71, 12.41 in the r , i , z , J , H , and K filters,

respectively. The estimated uncertainties are 0.05–0.1 mag in the Sloan bands, dominated by the image subtraction residuals, and 0.05–0.08 mag in the NIR filters. The observed broad band magnitudes constrain well the shape of the SED and indicate the companion is a late M star with $T_{\text{eff}} \approx 3200$ K. Unfortunately, we do not have an independent handle on the stellar radius that will allow us to determine the distance to the companion. If we assume it is a MS star, the R_{\star} can be estimated using the semi-empirical T_{eff} -radius relation derived by Mann et al. (2015). The nominal value from that relation is $R_{\star} = 0.25 R_{\odot}$, corresponding to a distance to the neighbor $D \approx 90$ pc. There is, however, a significant uncertainty ($\sim 15\%$) associated with the T_{eff} -radius relation leading to a substantial spread in distances. It is interesting to note that for $R_{\star} = 0.28 R_{\odot}$, i.e., only 1σ away from the nominal value, the estimated distance to the companion is the same as to the primary, $D \approx 100$ pc (see Figure 4) in which case the projected distance between the two stars would be ~ 450 AU.

To further test whether the two stars are possibly associated we place them on a color-magnitude diagram (CMD) using the *Gaia* G (DR1, Gaia collaboration 2016) and 2MASS J magnitudes. *Gaia* separates the two stars cleanly and lists their magnitudes as 11.076 and 15.982, respectively. For the J -band we use the 2MASS magnitude of the primary and our estimate of the companion magnitude based on the Keck AO images. Figure 7 shows the CMD for the two stars and a 1 Gyr theoretical isochrone from the Padova database (Marigo et al. 2017). The CMD clearly shows our estimates of the primary star parameters and the distance are close to the theoretically expected values for a 1 Gyr old star. The companion object, on the other hand, projects about 3σ away from the theoretical isochrone. At face value, the CMD does not support the association scenario; however, given the uncertainties and assumptions about the close-by star, we cannot draw any definite conclusion. Further investigation of possible association is be-

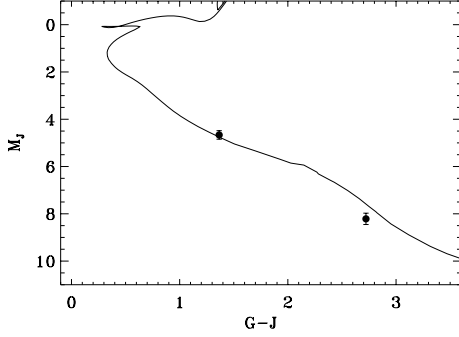


Figure 7. Color-magnitude diagram (*Gaia* $G - J$, J) for Qatar-6b host star and its neighbor for a distance $d = 101$ pc. Overplotted is a 1 Gyr isochrone from the Padova database (Marigo et al. 2017) assuming solar abundances. The error bars are dominated by the uncertainty in the distance estimate.

yond the scopes of this paper, and can be carried out much more reliably once the proper motion of both stars is measured by *Gaia*.

Eclipsing binaries, both projected and gravitationally bound, are the main source of false positive detections in transit surveys. Fortunately, this is not the case for Qatar-6b for two reasons. First, being more than 5 mag fainter, the companion object can not produce the observed transit depth of $\sim 2\%$ in the r and V bands. Second, the observed RVs, which are measured from the part of the spectrum covering the Sloan g and r bands, can only come from the primary star as the companion contributes $< 1\%$ to the combined light in this wavelength range. Thus, the observed RV curve reflects the orbital motion of the primary star only and it is at the same period as the transits.

3.4. Orbital period determination

To better determine the transiting planet ephemeris we used the data from the follow-up photometric curves. As described in a previous Section, we have observed 6 transits of Qatar-6b between January 30 and June 9, 2017, spanning 37 orbital cycles of the system. First, all observational time stamps were placed on the BJD_{TDB} system and each light curve was rebinned to a uniform ca-

Table 3. Central times of Qatar-6b transits and their uncertainties.

Transit central time $BJD_{TDB} - 2,400,000$	Cycle No.	Filter	Telescope/ Instrument
57784.03257 ± 0.00068	0	Sloan i	KeplerCam
57822.60106 ± 0.00076	11	V	Meade
57836.62569 ± 0.00048	15	V	Meade
57878.70010 ± 0.00043	27	Sloan i	KeplerCam
57892.72446 ± 0.00036	31	Sloan r	KeplerCam
57913.76215 ± 0.00047	37	Sloan z	KeplerCam

dence of 2 min for the KeplerCam observations and 2.5 min for the Meade LX200GPS observations, to reduce the error bars on individual points. When binning the errors were propagated assuming data points were uncorrelated and we checked that this level of binning did not affect derived parameters. Each individual light curve was then fitted with a transit model using EXOFAST (Eastman et al. 2013). We note that EXOFAST uses a wavelength dependent quadratic limb darkening prescription and uncertainties of the fitting parameters are estimated via Markov Chain Monte Carlo (MCMC) minimization.

The transit central times T_C and their uncertainties were estimated from the model fits and we calculated the best ephemeris by fitting a straight line through all the points. Figure 8 shows the fit and the residuals from the linear ephemeris, and the measurements of T_C and their uncertainties are summarized in Table 3. The final orbital ephemeris is expressed as

$$T_C = 2457784.03270(49) + 3.506195(18) E \quad (1)$$

where E is the number of cycles after the reference epoch, which we take to be the y-intercept of the linear fit, and the numbers in parenthesis denote the uncertainty of the last two digits of the preceding coefficient. Here the reference epoch and the period are in days on the BJD_{TDB} scale, and their un-

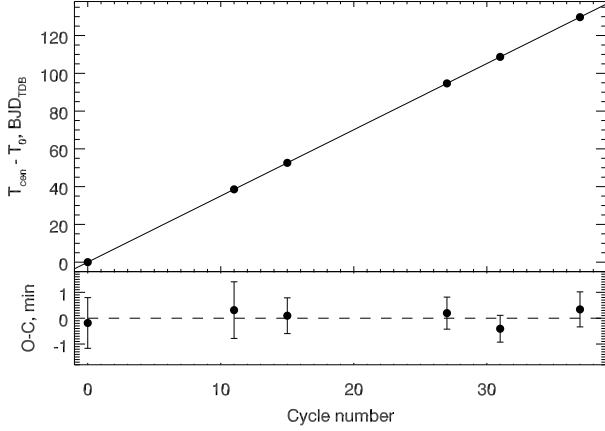


Figure 8. The orbital period for Qatar-6b and residuals of central transit times from a linear ephemeris.

certainties correspond to 42 s, and 2 s, respectively. The quality of the fit as measured by $\chi^2 = 1.11$ indicates that a linear ephemeris is a good match to the available measurements given the quality of the observations. Thus, an investigation of possible transit timing variations (TTV) would require data of much superior quality.

3.5. Planetary system parameters

To determine the physical parameters of the planetary system we run a global solution of the available RV and transit photometric data using version 2 of EXOFAST – a full re-write of the original package, designed to simultaneously fit RV and/or transit data for multiple planets, transits, and RV sources (Eastman 2017). Further description of EXOFASTv2 and similarities and differences with the original version can be found in Eastman et al. (2017) and Rodriguez et al. (2017). One major difference which is important in our case is that EXOFASTv2 uses the YY isochrones (Yi et al. 2001) to model the star, instead of the Torres relations (Torres et al. 2010), see also Eastman et al. (2016) for a more detailed description).

The global fit of Qatar-6b includes the RV measurements listed in Table 1 and the six follow-up photometric light curves shown in Figure 2. The stellar parameters (T_{eff} , $\log g$, $[m/H]$) determined from the spectroscopic analysis (Section 3.1) and

the orbital period and reference epoch measured from the analysis of the transit central times (Section 3.4) are fed as initial parameters for the global fit.

The spectroscopically determined stellar parameters and the comparison with the theoretical isochrones suggest that the host star is well positioned on the main sequence. Quadratic limb darkening coefficients (LDCs) were interpolated from the Claret & Bloemen (2011) tables for each filter and used as initial input. The LDCs were left free to vary, but we imposed a Gaussian prior around the interpolated value with an uncertainty of 0.05. An additional Gaussian prior was imposed on the stellar age, with a mean value of 1 Gyr and an uncertainty of 0.5 Gyr, based on our analysis in Section 3.1, while an upper-bound uniform prior of $A_V < 0.1$ was imposed on the visual extinction, as suggested by the Galactic dust reddening maps (Schlafly & Finkbeiner 2011).

With respect to the eccentricity, using the equations from Leconte et al. (2010) and Jackson et al. (2008), we calculated the tidal circularization time-scale for the system. We used the values from Table 4 of M_\star , R_\star , M_P , R_P , assuming tidal quality factors of $Q_\star = 10^{6.5}$ and $Q_P = 10^{5.5}$. The rotation period given in Table 4, $P_{\text{rot}} = 12.75$ d, is calculated using the stellar radius from our solution, the $v \sin i$ from the spectra, and assuming the stellar rotation axis and the planet orbit are coplanar. The time-scale for circularization is $\tau_{\text{circ}} = 0.08$ Gyr, significantly lower than the estimated age of the host star and, thus, we expect the planet orbit to have circularized. Additionally, our RV data is not of high enough quality to allow investigation of (any potential) small departures from circularity. For these reasons, in fitting the Qatar-6b data set, we only considered a circular orbit and kept the eccentricity fixed to zero.

Table 4 summarizes the physical parameters of the planetary system. The best fit for both radial velocity and photometric light curves is coming from the EXOFASTv2 global fit. The Safronov

number is not used in the current paper and is provided in Table 4 for completeness, as it may be useful for other studies. A plot of the posterior distributions from the MCMC fit for selected stellar and planetary parameters is presented in Figure 9 to demonstrate the quality of the fit. For the LDCs, the MCMC fits converge very close to the interpolated values from Claret & Bloemen (2011) with typical uncertainty of 0.05.

3.6. Orbit orientation and limb darkening effects

The shape of our follow-up transit curves suggested the planet is likely on a grazing transit. For each transiting planetary system there is a minimum inclination, i_{gr} , below which the transit is grazing, i.e. part of the planet disk's shadow will always be outside the stellar disk even at maximum coverage. This theoretical limit is given by Equation 2

$$\cos i_{gr} = \frac{R_{\star} - R_p}{a} \quad (2)$$

In the case of Qatar-6b, this limit is $i_{gr} = 86.16^\circ$, using the planetary radius and semi-major axis values from Table 4. On the other hand, the inclination we measure through the global model fit is $i = 86.06^\circ$. The transit is just grazing (considering the errorbars), thus the value of the planet radius we measure from the transiting light curves should be very close to its true value (Figure 10). Nevertheless, we need to make clear that, for a grazing transit, the value of the planet radius from the model fit should be taken as a lower limit.

To a first degree, the shape of a planetary transit light curve is determined by the ratio of the planet radius to the stellar radius, the orbit scale and the transit impact parameter. Stellar limb darkening (LD), although being a second order effect, also plays an important role, as it modifies the shape of the light curve and affects the transit depth. In addition, the changes to the shape of the light curve and the depth of the transit are both wavelength and impact parameter dependent. In the case of Qatar-6b, our data allow us to check if the observed

differences in the transit depth conform with the expected effects of the stellar limb darkening.

The effects of the LD have been the subject of a number of studies. Here we use the formalism of Cszimadia et al. (2013) (see their Appendix B), where the transit depth $\Delta F/F$ dependence on the impact parameter and wavelength can be written as

$$\frac{\Delta F}{F} = k^2 \frac{1 - u_1(1 - \mu) - u_2(1 - \mu)^2}{1 - \frac{u_1}{3} - \frac{u_2}{6}} \quad (3)$$

where $k = R_p/R_{\star}$ is the ratio of planet radius to star radius, and u_1 and u_2 are the linear and quadratic limb darkening coefficients. We also use the common notation $\mu = \cos \gamma$, where γ is the angle between the normal vector of the stellar surface point and the direction to the observer. It is easy to show that, at the time of maximum light loss, $\mu = \sqrt{1 - b^2}$, where b is the impact parameter. Keeping in mind that limb darkening coefficients are wavelength dependent, Equation 3 describes both the impact parameter and wavelength dependence of the transit depth.

The case of Qatar-6b is demonstrated in Figure 11. The left panel shows the expected radial profile of the central transit depth $\Delta F/F$ as a function of the impact parameter b , as approximated by Eq. 3. For a given value of b , the wavelength dependence of $\Delta F/F$ is apparent as different values for curves shown for V band (0.55μ , green), Sloan r (0.62μ , yellow), Sloan i (0.77μ , red), and Sloan z (0.92μ , black). The panel illustrates that for central transits (e.g., $b \lesssim 0.5$), the transit depth is expected to decrease with wavelength, while for grazing transits ($b \gtrsim 0.8$), it should increase with wavelength. The right panel of Figure 11 shows what we observe in Qatar-6b and it matches what is expected for a grazing transit. For clarity, only the model fits to the filter light curves are shown in matching colors as in the left panel. For Qatar-6b we measure central transit depth values of 0.0178, 0.0180, 0.0182, and 0.0192 for V , Sloan r , i , and z band filters, respectively. These compare reasonably well with

Table 4. Median values and 68% confidence intervals. We assume $R_{\odot}=696342.0$ km, $M_{\odot}=1.98855\times 10^{30}$ kg, $R_J = 69911.0$ km, $M_J=1.8986\times 10^{27}$ kg and 1 AU=149597870.7 km.

Parameter	Units	Qatar-6b
Stellar Parameters:		
M_*	Mass (M_{\odot})	0.822 ± 0.021
R_*	Radius (R_{\odot})	0.722 ± 0.020
L_*	Luminosity (L_{\odot})	0.306 ± 0.026
ρ_*	Density (g/cm^3)	3.08 ± 0.16
$\log(g_*)$.	Surface gravity (cgs)	4.636 ± 0.014
T_{eff}	Effective temperature (K)	5052 ± 66
[Fe/H].	Metallicity	-0.025 ± 0.093
τ_{YY} . . .	Age (Gyr)	1.02 ± 0.62
A_V	Extinction (mag)	0.05 ± 0.04
d_{SED} . . .	Distance (pc)	101.5 ± 5.6
Planetary Parameters:		
P	Period (days)	3.506189 ± 0.000020
a	Semi-major axis (AU)	0.0423 ± 0.0004
M_P	Mass (M_J)	0.668 ± 0.066
R_P	Radius (R_J)	1.062 ± 0.071
ρ_P	Density (g/cm^3)	0.68 ± 0.14
$\log(g_P)$	Surface gravity	3.162 ± 0.069
T_{eq}	Equilibrium Temperature (K) .	1006 ± 18
Θ	Safronov Number	0.064 ± 0.007
e	Eccentricity (fixed)	0
RV Parameters:		
K	RV semi-amplitude (m/s)	101.6 ± 9.6
γ_{rel}	Systemic velocity (m/s)	152.4 ± 7.8
Primary Transit Parameters:		
R_P/R_* .	Radius of planet in stellar radii	0.151 ± 0.007
a/R_* . . .	Semi-major axis in stellar radii	12.61 ± 0.22
i	Inclination (degrees)	86.01 ± 0.14
b	Impact Parameter	0.878 ± 0.016
T_{14}	Total duration (days)	0.0662 ± 0.0010

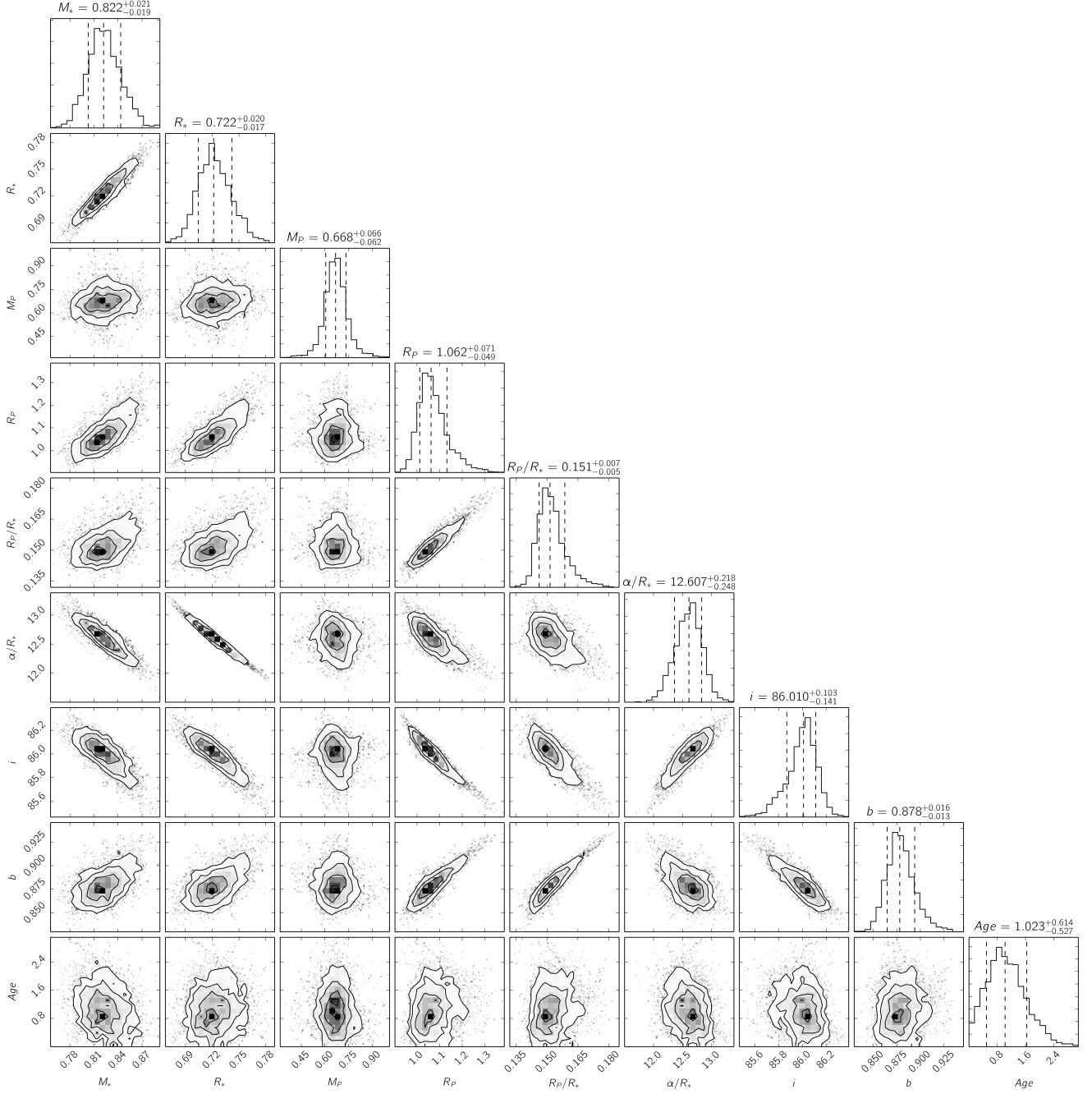


Figure 9. Corner plot of the posterior distributions from the MCMC fit for selected parameters of the Qatar-6b system.

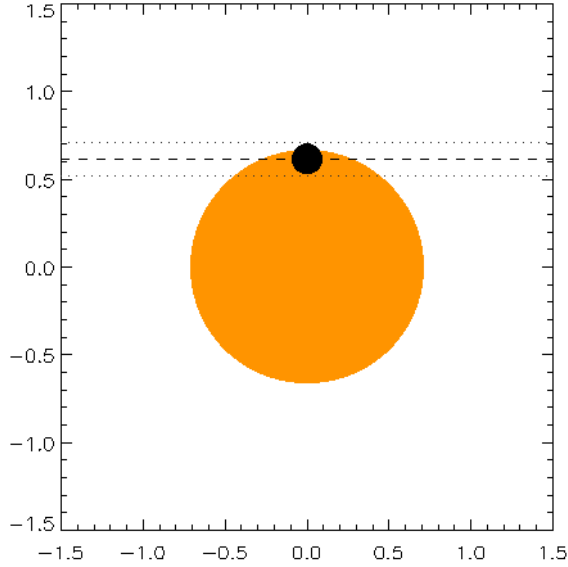


Figure 10. Orbital geometry for Qatar-6b, showing the grazing character of the transit. The figure is drawn to scale in units of solar radius.

the predicted values of 0.0185, 0.0190, 0.0196, and 0.0201 from Eq.3.

4. CONCLUSIONS

In this paper, we present the identification of Qatar-6b as a $0.65 M_J$ hot Jupiter, orbiting a $0.817 M_\odot$, early-K star, with a period of $P_{\text{orb}} \sim 3.5$ d. The age of the host star is estimated to be $\tau \sim 1$ Gyr, while an SED fit to available and measured multi-band photometry yields a distance of $d = 103$ pc to the system. From a global, simultaneous fit to our follow-up photometric and spectroscopic observations we measure the planet's radius as $R_p = 1.04 R_J$, and demonstrate that the transit is grazing, meaning that the R_p value should be taken as a lower limit only. We do, however, show that the true value of the planetary radius should not be too far off. We also investigate the nature of a neighboring object, next to the host star, and conclude that its presence is in no way related to the observed periodic variability of Qatar-6b's host and does not affect the estimated planetary parameters.

Qatar-6b joins the small family of (nearly) grazing transiting planets. The huge difference in numbers between fully and grazing transiting planets is somewhat puzzling. It is true that the shape of grazing transits is almost perfectly mimicked by blended eclipsing binaries, so the small numbers of grazing exoplanets can (at least partially) be attributed to a selection effect, i.e., cases of mistaken false-positive identifications (Brown 2003). However, Oshagh et al. (2015) note that the numbers of grazing exoplanets are still lower than expected and propose a physical mechanism where the transit depth of a grazing exoplanet diminishes below the detection threshold, under the assumption that the host star harbors a giant polar spot. As such, increasing the numbers of known grazing exoplanets is important to better understand these detection biases and any potential mechanism behind them.

And finally, planets in grazing transit configurations are especially valuable as they are potentially the best targets to look for the presence of additional bodies in their systems that would lead to detectable variations in the transit impact parameter and duration (Kipping 2009, Kipping 2010). These would require high cadence and high photometric accuracy observations that could be achieved with large ground based telescopes and/or space based facilities.

ACKNOWLEDGEMENTS

This publication is supported by NPRP grant no. X-019-1-006 from the Qatar National Research Fund (a member of Qatar Foundation). The statements made herein are solely the responsibility of the authors. ZT thanks Jason Eastman for his help in installing and de-bugging the beta version of EXOFASTv2 and for the extensive discussions on applying different priors and their impact on the global fit. C.B. acknowledges support from the Alfred P. Sloan Foundation. Some of the data presented herein were obtained at the W. M. Keck Observatory, which is operated as a scientific partnership among the California Institute of Technology, the University of California

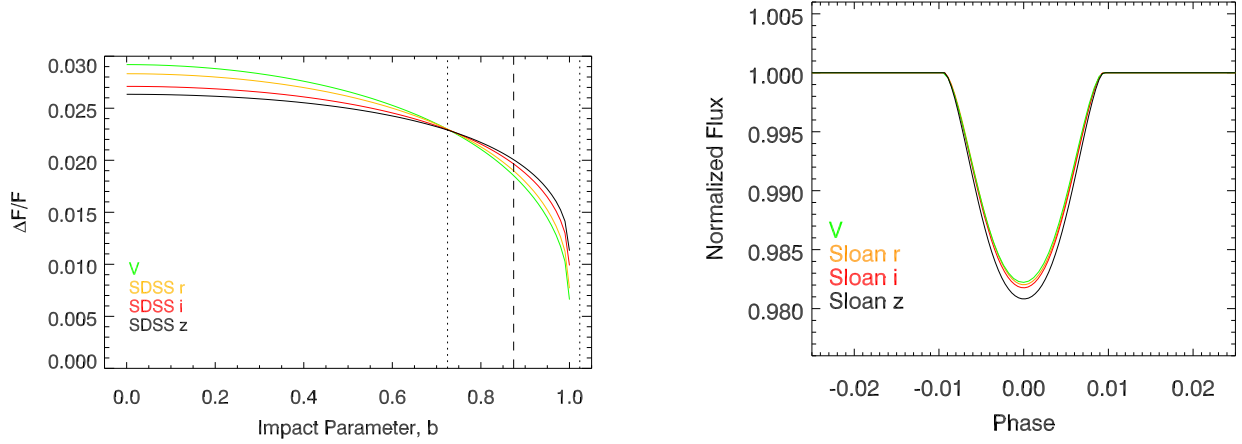


Figure 11. *Left panel:* Predicted radial profile of the central transit depth $\Delta F/F$ as a function of impact parameter (Eq.3). Vertical lines denote the positions of the center (dashed) and two edges (dotted) of the planet disk. *Right panel:* Observed transit depths for Qatar-6b as a function of wavelength. Because of the grazing geometry the transit depth is increasing with wavelength as expected.

and the National Aeronautics and Space Administration. The Observatory was made possible by the generous financial support of the W. M. Keck Foundation. AE is supported by the National Natural Science Foundation of China (grant no. 11273051). This work has made use of data

from the European Space Agency (ESA) mission *Gaia* (<https://www.cosmos.esa.int/gaia>), processed by the *Gaia* Data Processing and Analysis Consortium (DPAC, <https://www.cosmos.esa.int/web/gaia/dpac/consortium>). Funding for the DPAC has been provided by national institutions, in particular the institutions participating in the *Gaia* Multilateral Agreement.

REFERENCES

- Agol E. et al., 2005, MNRAS, 359, 567
 Albareti R. et al, 2016, arXiv:1608.02013
 Albrecht S. et al., 2012, ApJ, 757, 18A
 Almenara, J. M. et al. 2013, A&A, 555, A118
 Almenara, J. M. et al. 2015, A&A, 575, A71
 Alsubai K. et al. 2013, Acta Astron., 63, 465
 Alsubai K. et al. 2017, ApJ, 153, 200
 Anderson, D. R. et al. 2011, PASP, 123, 555
 Anderson, D. R. et al. 2012, MNRAS, 422, 1988
 Barbary, K., 2016, The Journal of Open Source Software, 1
 Béky B. et al. 2011, ApJ, 734, 109
 Bertin, E., Arnouts, S., 1996, A&AS, 117, 393
 Bessell, M. S. 2000, PASP, 112, 961
 Bramich D. M. 2008, MNRAS, 386, L77
 Brown D. J. A. 2014, MNRAS, 442, 1844
 Brown, T. M. 2003, ApJL, 593, L125
 Buchhave L. A. et al., 2010, ApJ, 720, 1118
 Buchhave L. A. et al., 2012, Nature, 486, 375
 Castelli F. & Kurucz, R. L., 2004, astro-ph/0405087
 Charbonneau D. et al, 2002, ApJ, 568, 377
 Charbonneau D. et al, 2005, ApJ, 626, 523
 Claret A. & Bloemen, S., 2011, A&A, 529, 75
 Collier Cameron A. et al. 2006, MNRAS, 373, 799C
 Craig, M. W. et al. 2015, Astrophysics Source Code Library, ascl, 1510.007
 Cszimadia Sz. et al. 2013, A&A, 549, A9
 Cszimadia Sz. et al. 2015, A&A, 584, 13
 Deming D. et al., 2005, Nature, 434, 740
 Deming D. et al., 2006, ApJ, 644, 560
 Dotter A. et al., 2008, ApJS, 178, 89
 Droege T. F. et al., 2006, PASP, 118, 1666
 Eastman J., 2017, private communication
 Eastman J., Gaudi B.S., & Agol E., 2013, PASP, 125, 83
 Eastman J. et al., 2016, AJ, 151, 45
 Eastman J. et al., 2017, ApJ, in press
 Grziwa S. et al., 2016, AJ, 152, 132

- Gaia collaboration, 2016, *A&A*, 595, A2
Hellier C. et al., 2012, *MNRAS*, 426, 739
Hellier C. et al., 2017, *MNRAS*, 465, 3693
Holman M. J., Murray N. W., 2005, *Sci*, 307, 1288
Jackson B., Greenberg R., & Barnes R., 2008, *ApJ*, 678, 1396
Kipping D. M., 2009, *MNRAS*, 396, 1797
Kipping D. M., 2010, *MNRAS*, 407, 301
Kovács G., Bakos G. and Noyes R., 2005, *MNRAS*, 356, 557
Kovács G., Zucker S. & Mazeh T., 2002, *A&A*, 391, 369
Leconte J., Chabrier G., Baraffe I., Levrard B., 2010, *A&A*, 516, 64
Lillo-Box J. et al, 2015, *A&A*, 577, A105
Marigo, P., et al. 2017, *ApJ*, 835, 77
Mann A. W. et al. 2015, *ApJ*, 804, 64
McCormac J. et al. 2014, *MNRAS*, 438, 3383
Mislis, D., Pyrzas, S., Alsubai, K. A. et al. 2017, *MNRAS*, 465, 3759M
Oshagh, M. et al. 2015, *A&A*, 583, L1
Pecaut M. J. & Mamajek E. E., 2013, *ApJS*, 208, 9
Pickles A. & Depagne E., 2010, *PASP*, 122, 1437
Rodriguez J. E. et al., 2017, *AJ*, 153, 256
Schlafly E. F. & Finkbeiner D. P., 2011, *ApJ*, 737, 103
Service M. et al, 2016, *PASP*, 128, 500
Sing D. K. et al., 2016, *Nature*, 529, 59
Smalley B. et al., 2011, *A&A*, 526, A130
Tinetti G. et al., 2007, *Nat*, 448, 169
Torres G., Andersen J. and Giménez A., 2010, *A&ARv*, 18, 67
Winn J. N., Fabrycky D. C., 2015, *ARA&A*, 53, 409
Yi S., Demarque, P., Kim Y.-C. et al., 2001, *ApJS*, 136, 417